Digital Object Identifier 10.1109/TPEL.2024.3365850

IEEE Transactions on Power Electronics

An Enhanced Model Predictive Capacitor Voltage Control of Hybrid Modular Multilevel Converters Under Overmodulation Circumstances

Amin Hashemi-Zadeh
Saeid Ahmadi
Yousef Neyshabouri
Ehsan Asadi
Hossein Iman-Eini
Marco Liserre

Suggested Citation

A. Hashemi-Zadeh, S. Ahmadi, Y. Neyshabouri, E. Asadi, H. Iman-Eini and M. Liserre, "An Enhanced Model Predictive Capacitor Voltage Control of Hybrid Modular Multilevel Converters Under Overmodulation Circumstances," in IEEE Transactions on Power Electronics, vol. 39, no. 6, pp. 7130-7143, June 2024

An Enhanced Model Predictive Capacitor Voltage Control of Hybrid Modular Multilevel Converters Under Over-Modulation Circumstances

Amin Hashemi Zadeh, Saeid Ahmadi, Yousef Neyshabouri, Ehsan Asadi, Hossein Iman-Eini, and Marco Liserre

***Abstract*— Modular multilevel converters (MMCs) require well-balanced submodule (SM) capacitor voltages at the reference value for satisfactory steady-state and dynamic operations. Achieving this goal in hybrid MMCs, where the modulation index exceeds one, becomes intricate owing to the differing participation of half-bridge SMs (HB-SMs) and full-bridge SMs (FB-SMs) in arm voltage generation. This paper proposes an advanced voltage balancing method based on enhanced phase-shift modulation and model predictive control, featuring a single comprehensive cost function that utilizes a novel form of redundancy to manage the insertion of HB- and FB-SMs in a wide range of modulation indices. The designed cost function addresses four key control objectives: inter-cell balancing by tracking the DC voltage reference, minimizing the energy deviation between the HB- and FB-SMs, inter-leg balancing to eliminate energy variations between the upper and lower arms, and rejecting voltage errors arising from uncertainties in the SM capacitance using a Kalman filter (KF)-based observer. This method enables comprehensive capacitor voltage balancing, which is suitable for various modulation indices and power factors. The validity of the proposed method is substantiated through simulations using MATLAB/SIMULINK software and experiments conducted on a scaled-down hardware prototype.**

Index Terms*—*Capacitor voltage balancing, hybrid modular multilevel converters, model predictive control, overmodulation circumstances.

I. Introduction

Modular multilevel converters have become increasingly popular over the past decade due to their remarkable advantages, including high efficiency, scalability, modularity, high quality output voltage, excellent output quantization, and elimination of bulky filters and shift transformers [1], [2]. Therefore, the use of MMC is rapidly growing across a wide range of high-power applications, such as high-voltage direct-current systems (HVDC), microgrids, static synchronous compensators (STATCOM), and medium voltage drives [3-6]. Each application has challenges, especially concerning DC fault-handling, which is especially important in multiterminal HVDC transmission networks and overhead line transmission, where DC short-circuit faults are prevalent [7]. The conventional MMC structure lacks inherent fault clearance capability owing to the limited capacity of HB-SMs to generate negative voltages [8].

Typical methods for isolating DC faults recommend circuit breakers (ac or DC) and bypass cells with thyristors. However, both approaches are time-consuming and costly [9-11]. One straightforward solution to achieve inherent fault-handling capability is to replace all HB-SMs with FB-SMs. Nevertheless, this strategy doubles the number of active switches, escalating power dissipation and posing manufacturing expenses [12].

Alternatively, the hybrid MMC combines HB- and FB-SMs to attain a promising compromise between power losses, cost issues, and handling DC faults [10-12]. An intriguing point regarding hybrid MMCs is that the inclusion of FB-SMs within the arms introduces a novel aspect of flexibility by enabling the generation of negative voltage levels. This attribute permits the ac output voltage to exceed half the DC-link voltage. Consequently, accommodating modulation indices beyond unity (the overmodulation capability) becomes feasible. Hybrid MMCs equipped with this overmodulation capability yield remarkable benefits, which are briefly outlined as follows:

1. DC fault handling capability:

Hybrid MMCs composed of mixed HB- and FB-SMs can be a trade-off between DC fault protection, cost, and conduction losses [13], [14]. During fault instant, the utilized FB-SMs can insert a negative voltage to limit the energy fed to the faulty point.

2. Enhanced operation under DC link variations:

The hybrid MMC exhibits resilience in the face of challenges such as extreme weather, insulator failure, and de-icing, which can decrease the DC voltage on the HVDC side [15], [16]. The hybrid MMC maintains a constant ac voltage despite reducing the DC input by utilizing its overmodulation capability.

3. Increased power transmission capability:

Hybrid MMCs enhance the power rating during bidirectional AC–DC conversion. Authors in [17] show that at $M = \sqrt{2}$, the maximum active power is transferred. In addition, hybrid MMCs offer an output voltage of higher quality owing to the extra negative voltage level generated by FB-SMs [10], [11].

Despite the abovementioned merits, under overmodulation conditions, the voltage imbalanced issue emerges because HB- and FB-SMs hold unequal charging and discharging properties, resulting in unstable capacitor voltage. More specifically, FB-SMs can be energized and de-energized irrespective of the current direction of the arms. Conversely, HB-SMs accept only positive and negative arm currents. Because the negative arm current remains available for a shorter time as the modulation index increases, the discharge of HB-SMs is constrained [10-16].

Several studies in the literature have been presented to address the voltage imbalance issue in hybrid MMCs. In [12], a simple solution is suggested: increasing the insertion index of FB-SMs to compensate for the voltage deviation among HB and

FB-SMs. Such methods increase power dissipation and highlight the cost issue. In a different genre, the voltage imbalanced issue in MMCs is tackled with a self-balancing branch structure [18]. Scholars in [19] introduce a power circuit to remove voltage imbalances autonomously in hybrid MMCs. Despite well-satisfied balancing and mitigating power losses, it supplements the component counts and complicates the circuit design by considering additional power components. The remaining strategies in the literature can be divided into two main categories. The first prioritizes active SMs based on adjunct analysis to adapt the capacitor voltage sorting algorithm. A sorting and balancing algorithm suitable for overmodulation conditions is presented in [20], which increases the power transmission capability by reducing the HB-SMs switching frequency. According to [10], an energy-based modification approach eliminates cell energy variations by combining the sorting algorithm with energy analysis. Although reactive power ensures sufficient charging or discharging interval for the HB-SMs, it increases the amplitude of arm and phase currents, causing higher losses. Generally, methods based on voltage sorting algorithms are subject to increased frequency of switching power devices [21], [22].

The second category concentrates on energy analysis to calculate the appropriate magnitude and phase angle of the circulating current. Balanced capacitor voltages with reduced ripples are obtained by injecting the determined circulating current into the converter. While [23] and [24] employ the circulating current with fundamental frequency, the authors in [11] and [25] do the same with a second-order frequency. Some other references, such as [26], also use third-order frequency to minimize energy fluctuations in SMs. The precise calculation of the reference value for the circulating current is a challenging task, as any uncertainty in this determination could potentially compromise the operational performance of the hybrid MMC, particularly if the injected circulating current falls short of meeting the voltage balancing requirements.

Further investigation is imperative to address the voltage imbalance issue in hybrid MMC to exploit FB-SMs efficiently. Therefore, this study aims to develop an inclusive voltage balancing control scheme that enhances converter performance characteristics in steady-state and transitional conditions. The proposed control method uses a new form of redundancy in a model predictive control (MPC) scheme to adjust the insertion of HB- and FB-SMs. A single cost function is developed covering different aspects of voltage balancing in the hybrid MMC: inter-cell voltage balancing, minimizing voltage fluctuations of HB- and FB-SMs, inter-leg balancing, and robustness to uncertainties in SM capacitance. The last term is achieved by employing a KF observer, which estimates the error caused by the mentioned uncertainties.

The proposed method outperforms the existing approaches by ensuring reliable capacitor voltage balancing while minimizing tracking errors and voltage ripples across a broad spectrum of extended operational regions. The proposed control strategy utilizes a new form of redundancy for better voltage balancing without sorting algorithms, PI regulators, or circulating current injections. Additionally, the proposed control approach exhibits resilience in the presence of changes in the SM capacitance. The contributions of this study are summarized as follows.

1. Using a hybrid combination of enhanced phase-shift modulation and MPC to achieve an energy balance between each arm's HB and FB submodules, the energy balance between the upper and lower arms (i.e., vertical energy balance), and different phases (i.e., horizontal energy balance).
2. Achieving high-performance voltage balancing with low reference tracing errors and ripples across an extensive working region under overmodulation conditions.
3. Improving converter performance by introducing a novel form of redundancy and designing for robustness against uncertainties in module capacitance.

The remainder of the paper is organized as follows. Section II discusses the fundamental equations of hybrid MMC and introduces the new type of redundancy. Section III explains the proposed control scheme, covering topics such as the developed cost function for the MPC and the design of an observer for disturbance rejection. Sections IV and V present the simulation and experimental results, respectively, and Section VI concludes the paper.

II. The Principle of Operation and New Redundancies

A. Configuration and equations

Figure 1 illustrates the three-phase hybrid MMC configuration. L_{arm} and R_{arm} denote the inductance and resistance of the arms, respectively. In addition, there are N SMs in each arm, out of which F is the number of FB types and the remainder are HB. The HB- and FB-SMs capacitances are considered the same, denoted by C. V_{dc} stands for the voltage of the DC link. Furthermore, v_p and $i_p$are output voltage and current, respectively, where $p \in \{a,b,c\}$.

Regarding the analytical study of the hybrid MMC [4], the upper and lower arm voltages for phase a can be expressed as

$$\begin{cases} v_{ua} = \frac{V_{dc}}{2}(1 - Msin\omega t) \\ v_{la} = \frac{V_{dc}}{2}(1 + Msin\omega t) \end{cases} \tag{1}$$

where M is the modulation index, and ω is the fundamental angular frequency. Since the voltage drop due to the arm resistance and inductance is insignificant, the output voltage in phase-a can be expressed as

$$v_o = \frac{v_{la} - v_{ua}}{2} = \frac{MV_{dc}}{2} sin\omega t = v_{ma} sin\omega t \tag{2}$$

where v_{ma} is the output voltage amplitude. Furthermore, the upper and lower arm currents are

$$\begin{cases} i_{ua} = i_{cira} + \frac{i_a}{2} \\ i_{la} = i_{cira} - \frac{i_a}{2} \end{cases} \tag{3}$$

where i_a is the ac output current which is obtained as

$$i_a = i_{ma} sin\,(\omega t - \varphi) \tag{4}$$

where i_{ma} denotes the current amplitude, and φ is the phase angle of the load. Additionally, i_{cira} is the circulating current and formulated as

$$i_{cira} = \frac{I_{dc}}{3} + i_{cira}{}^{(ac)} \tag{5}$$

involving DC and ac components. Furthermore, the converter input and output powers are

$$\begin{cases} P_{out} = \frac{3}{2} v_{ma} i_{ma} cos\varphi \\ P_{in} = V_{dc} I_{dc} \end{cases} \tag{6}$$

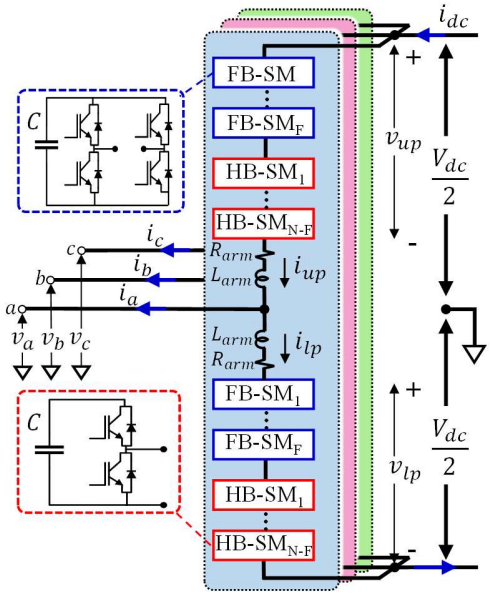

Fig. 1. Three-phase H-MMC Configuration.

which can be assumed to be equal by ignoring the power losses. From (6) and (2), the DC link current is derived as

$$I_{dc} = \frac{3}{4} M i_{ma} cos\varphi. \tag{7}$$

By inserting (4), (5), and (7) into (3) and neglecting the ac term of circulating currents, the arm currents are calculated per

$$\begin{cases} i_{ua} = \frac{1}{4} M i_{ma} cos\varphi + \frac{1}{2}\, i_{ma} \sin(\omega t - \varphi) \\ i_{la} = \frac{1}{4} M i_{ma} cos\varphi - \frac{1}{2}\, i_{ma} \sin(\omega t - \varphi) \end{cases}. \tag{8}$$

The negative section of the arm currents narrows upon increasing the modulation index. Similarly, as the power factor increases, the period during which the arm currents are positive is expanded. Hence, the most demanding balancing conditions emerge when modulation indices and power factors approach one.

B.Extended Operation Region

The proportion of FB-SMs to the total SMs in each arm defines the hybrid ratio as a determining factor of the correlation between the DC input and ac output, that is

$$h = \frac{F}{N}. \tag{9}$$

The maximum and minimum values of the upper arm voltage are formulated as

$$\begin{cases} v_{u/l,max} = NV_c \\ v_{u/l,min} = -FV_c \end{cases} \tag{10}$$

where V_c is the capacitor voltage of SM. The upper arm voltage reaches the highest level when all SMs generate a positive output voltage. In contrast, its minimum value happens when all FB-SMs engage in generating the arm voltage with negative output. Since the arm voltages vary between $-FV_c$ and NV_c, the DC term of arm voltages in (1) should follow the average value of these two limits, i.e.,

$$\frac{V_{dc}}{2} = \frac{(N-F)V_c}{2}. \tag{11}$$

This means that $V_c = V_{dc}/(N-F)$. Now by inserting V_c into (10), and considering the extreme values of arm voltages in (1), the maximum modulation index is obtained in terms of h as

$$M_{max} = \frac{N+F}{N-F} = \frac{1+h}{1-h}. \tag{12}$$

TABLE I
ADDITIONAL SWITCHING STATES OF HYBRID MMC FOR TWO HYBRID RATIO

L	h	S_{u1}^{hb}	S_{u2}^{hb}	S_{u3}^{hb}	S_{u1}^{fb}
0	0.25	1	0	0	-1
		0	1	0	-1
		0	0	1	-1
	0.5	1	0	-1	0
		0	1	-1	0
		0	0	-1	1
		1	0	0	-1
		0	1	0	-1
		0	0	1	-1
		1	1	-1	-1
1	0.25	1	1	0	-1
		1	0	1	-1
		0	1	1	-1
	0.5	1	1	-1	0
		1	0	-1	1
		0	1	-1	1
		1	0	1	-1
		1	1	0	-1
		0	1	1	-1
2	0.25	1	1	1	-1
	0.5	1	1	-1	1
		1	1	1	-1
-1,3,4	0.25,0.5	-			

Fault-tolerance requirements determine the hybrid ratio "h"; however, its increment contradicts the primary purpose of mixing HB-SMs with FB-SMs because the higher the ratio, the more FB-SMs are in the arms. The benefits of hybrid MMC fading depend on increased power losses and component counts caused by a large number of FB-SMs.

C. Redundancies

In hybrid MMCs, if the modulation index is less than one, the FB-SMs operate identically to the HB-SMs. The number of switching states in this scenario is

$$S_{total} = \sum_{L=0}^{N} \binom{N}{L} \tag{13}$$

where N is the total number of SMs in the arms, and L is the desired voltage level. Including FB-SMs enables freedom in generating negative voltage in the arms. In this study, this extra option is employed to create a new form of redundancy for yielding voltage levels from $-F$ to N. The sum of the augmented redundancies by taking this approach is calculated as

$$S^*_{(L,q)} = \begin{cases} \sum_{L=0}^{N} \binom{N-F}{L+F}, & F = q \\ \sum_{L=0}^{N} \sum_{q=1}^{F-1} \binom{N-q}{L+q} \binom{F}{q} & F \neq q \end{cases} \tag{14}$$

where q is the number of inserted FB-SMs. For cases that the $S^*_{(L,q)}$ is undefined, there is no available options offered by the new form of redundancy. Otherwise, the calculated number from (14) gives the number of additional switching states to generate a specific voltage level. As a simple example, in an HB-MMC with $N = 4$, merely one selection is possible for having $L = 0$ in the arms, bypassing all cells, whereas, in a hybrid MMC with $N = 4$ and $h = 0.25$, the same voltage level can be generated by inserting an FB-SM with negative output and one of the three HB-SMs with a positive voltage. In both cases, the generated voltage levels are the same. Iterating this process clarifies the array of alternative switching

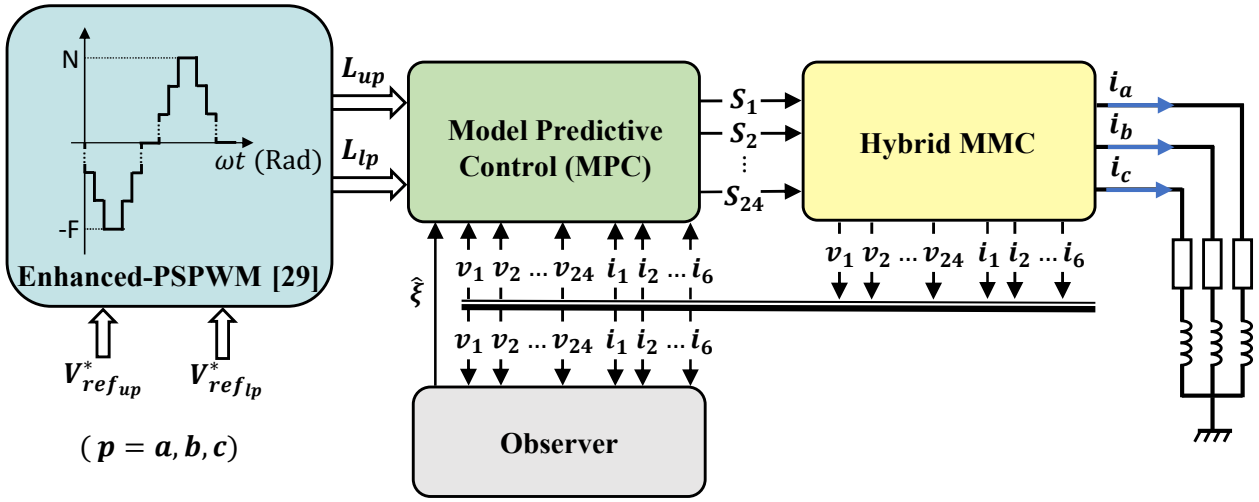

Fig. 2. Proposed Voltage Balancing Control Scheme Overview.

states for different voltage levels. This, in turn, enhances the efficiency of the charge and discharge cycles, enabling FB-SMs to cover the full arm voltage range. Table I compares the redundancies of the two designs for $N = 4$. The switching state of the i^{th} HB- and FB-SM in the upper arm is denoted by S_{ui}^{hb} and S_{ui}^{fb}, respectively.

III. Proposed Model-Predictive Control Scheme

Some classical control methods employ PI controllers for MMCs, which can be challenging for multiple PI control loops, particularly when multi-objective regulation is required. When applied to hybrid MMCs, they may not provide fast and accurate control during transients or lose stability in over-modulation regions. Because of these limitations, researchers have investigated modern control methods. Model predictive control (MPC) has become popular for MMCs owing to its ease of implementation, ability to control multiple objectives, fast dynamic response, and the capacity to handle nonlinearities and constraints. MPC is especially suitable for MIMO systems, such as MMC, compared to conventional methods [27], [28]. Furthermore, operating under overmodulation brings the converter closer to unstable performance. To avoid these difficulties, we developed a method based on Enhanced Phase-Shift Pulse-Width Modulation (EPS-PWM) and Direct MPC (DMPC) to achieve better and more stable performance in over-modulation conditions.

The DMPC approach optimizes a cost function that facilitates the attainment of all control objectives. In contrast, the Indirect MPC (IMPC) technique separates the control of the SM capacitor voltages from its cost function. Instead, it relies on an external voltage-sorting algorithm to ensure the equilibrium of the capacitor voltages. Fig. 2 presents an overview of the proposed voltage-balancing control scheme, where EPS-PWM, as detailed in [29], governs the desired voltage levels within each arm. Importantly, the role of this modulator does not include determining switching instants. Instead, it specifies the desired voltage level for each arm. Then, the MPC block is considered with extra redundancies to apply optimal switching states through the minimization of a Root Mean Squared Error single-cost function, formulated as

$$J = \Big[w_1 \left| V_c^*(k+1) - V_{cip}(k+1) \right|^2 + w_2 \left| \Delta \widetilde{W}^*(k+1) - \Delta \widetilde{W}_{u/l,p}(k+1) \right|^2 + w_3 \left| \Delta^* W(k+1) - \Delta W_p(k+1) \right|^2 + w_4 \left| \xi^*(k+1) - \xi_p^*(k+1) \right|^2 \Big]^{1/2} \quad (15)$$

In (15), four terms constitute the weighted cost function, each involving the predicted and extrapolated control variables. The prime control objective is to regulate capacitor voltages at a nominal DC reference, while the second objective is to remove energy variation in arms between HB- and FB-SMs. The third term concerns the energy balance between the upper and lower arm in each phase, and the fourth term considers robustness. The observer plays a part in the control system by estimating the disturbance resulting from the uncertainty in the capacitance of SMs. Each of these components is elaborated on separately in the forthcoming sections. As in the previous section, the equations are explained for phase a.

A. Capacitor voltage balancing in arms

A capacitor voltage can be equivalently modeled by DC and ac components as

$$v_{cia} = V_{cn} + \tilde{v}_{cia} \quad (16)$$

where V_{cn} is the nominal value, and $\tilde{v}_{cia}$ is an oscillating term involving high-order components. The discretized differential equation of the capacitor voltages derived by using forward Euler approximation is written as

$$v_{cia}(k+1) = v_{cia}(k) \pm \frac{T_s}{C} S_{ia}(k) i_{u/l,a}(k) \quad (17)$$

where T_s and C are the sampling time. Additionally, $S_{ia}(k)$ is the state of i_{th} module (that can be HB- or FB-SM) and the $V_{cia}(k+1)$ is the next state of capacitor voltage obtained from the present state of capacitor voltage $V_{cia}(k)$ and the multiplication of the arm current and the switching state, expressed in $S_{ia}(k) i_{u/l,a}(k)$. The sign is positive when SMs are inserted with a positive output voltage and negative for FB-SMs when the negative voltage is generated in the arms. The capacitor voltage reference relates to the DC link voltage and SM counts and is extrapolated as

$$v_c^*(k+1) = \frac{V_{dc}}{N-F}. \quad (18)$$

As a result, the prime control objective is included in the cost function as

$$J_1 = \left|V_c^*(k+1) - V_{cip}(k+1)\right|^2 \tag{19}$$

B. Inter-cell energy balancing

The dissimilar charging and discharging characteristics of HB- and FB-SM in an arm result in distinct voltage ripple patterns between them, which must be kept under control. If left unaddressed, this phenomenon increases the voltage stress of power switches and degrades the converter's performance. Moreover, it may prevent the ac output voltage from rising, especially when FB-SMs generate a negative voltage for an extended period and the arm currents are relatively short in the negative segment. Therefore, it is imperative to suppress the fluctuating energy between HB- and FB-SMs in the arms to reduce capacitor voltage ripples and, consequently, capacitor size and volume.

Given that the first control objective in the cost function is to regulate capacitor voltages at the nominal DC reference or to achieve equal energy distribution among SMs of the same type, the rate of change in the fluctuating energy of both the HB- and FB-SM in the upper arm can be written as

$$\begin{cases} \frac{dW_{uha}}{dt} = \frac{1}{N-F} p_{uha} \\ \frac{dW_{ufa}}{dt} = \frac{1}{F} p_{ufa} \end{cases} \tag{20}$$

where P_{uha} and P_{ufa} are the delivered instantaneous power to series HB- and FB-SMs, obtained as

$$\begin{cases} p_{uha} = v_{uha} i_{ua} \\ p_{ufa} = v_{ufa} i_{ua} \end{cases} \tag{21}$$

where v_{uha} and v_{ufa} are the total synthesized voltage of HB-SMs and FB-SMs, calculated as

$$\begin{cases} v_{uha} = \sum_{i=1}^{N-F} S_{ui}^{hb} V_c \\ v_{ufa} = \sum_{j=1}^{F} S_{uj}^{fb} V_c = (L_{ua} - \sum_{i=1}^{N-F} S_{ui}^{hb}) V_c \end{cases} \tag{22}$$

where S_{ui}^{hb} denotes the state of HB-SMs and can be 1 or 0, while S_{ui}^{fb} denotes the state of FB-SMs, which can be 1, 0, or -1. L_{ua} represents the voltage level, which EPS-PWM has determined for the upper arm-a. By subtracting the equations in (20), (21), and considering (22), the differential equation of the energy difference between HB- and FB-SM can be written as

$$\frac{d\Delta\widetilde{W}_{ua}(k)}{dt} = \frac{1}{N-F}\sum_{i=1}^{N-F} S_{ui}^{hb} - \frac{1}{F}\left(L_{ua} - \sum_{i=1}^{N-F} S_{ui}^{hb}\right) V_c i_{ua} \tag{23}$$

According to (23), the districted time model is calculated as

$$\Delta\widetilde{W}_{ua}(k+1) = \Delta\widetilde{W}_{ua}(k) + \frac{T_s}{N-F}\sum_{i=1}^{N-F} S_{ui}^{hb} - \frac{T_s}{F}\left(L_{ua}(k) - \sum_{i=1}^{N-F} S_{ui}^{hb}\right) V_c i_{ua}(k) \tag{24}$$

where $\Delta\widetilde{W}_{ua}(k)$ is the current state of the energy difference between HB- and FB-SM, which is calculated as

$$\Delta\widetilde{W}_{ua}(k) = \frac{W_{uha(k)}}{N-F} - \frac{W_{ufa(k)}}{F} \tag{25}$$

where $W_{uha}(k)$ and $W_{ufa}(k)$ are the stored energy of all HB- and FB-SMs at instant *k*, respectively. The proposed control scheme aims to alleviate the energy deviation between HB-SMs and FB-SMs by optimizing the selected switching state from available redundancies, as explained in Table 1. Finally, the corresponding term in the cost function is defined as

$$J_2 = \left|\Delta\widetilde{W}^*(k+1) - \Delta\widetilde{W}_{u/l,p}(k+1)\right|^2. \tag{26}$$

where $\Delta\widetilde{W}^*(k+1)$ is the estimated reference value, which must be set to zero.

C. Inter-leg Energy balancing

Attaining an energy balance between HB- and FB-SMs within the upper and lower arms does not always imply that different arms absorb the same amount of energy. Considering this, deviations in the sum of the capacitor voltages of the arms caused by energy imbalance are considerable. Theoretically, the power factor and modulation index are the reasons for this; however, in practice, asymmetrical converter parameters and component tolerations may cause such an imbalance. The pattern of change in the energy of the arms is formulated as

$$\frac{dW_{u/l,a}}{dt} = v_{u/l,a} i_{u/l,a} \tag{27}$$

where W_{ua} and W_{la} are the total amount of stored energy in upper and lower arms. Then, the difference derivatives between arm energies is

$$\frac{d\Delta W_a}{dt} = v_{ua} i_{ua} - v_{la} i_{la} \tag{28}$$

in which upper and lower arm voltages can be rewritten by the sum and difference of them as

$$v_{\sum/\Delta,a} = v_{ua} \pm v_{la}. \tag{29}$$

By replacing (3) and (29) in (28), the new relationship is achieved as

$$\frac{d\Delta W_a}{dt} = v_{\sum a}\frac{i_a}{2} + v_{\Delta a} i_{cira.} \tag{30}$$

As a result, the discretized equation is obtained as

$$\Delta W_a(k+1) = \Delta W_a(k) + T_s\left(v_{\sum a}(k)\frac{i_a(k)}{2} + v_{\Delta a}(k) i_{cira}(k)\right) \tag{31}$$

where $\Delta W_a(k+1)$ is the next state of energy variation between arms. Its reference, $\Delta^* W(k+1)$ must be set to zero. Accordingly, the following cost function term is derived as

$$J_3 = w_3\left|\Delta^* W(k+1) - \Delta W_p(k+1)\right|^2 \tag{32}$$

D. Robust Design

Despite the inter-cell and inter-arm balancing controls, the proper performance of the converter may be at risk because of the mismatch in the capacitance of SMs, degrading the operation of the capacitor voltage balancing. Motivated by this challenge, an additional observer is designed, which estimates the lumped disturbance caused by such uncertainties. The MPC compensates for this computed value and ensures the voltage balancing robustness.

Initially, the differential equation of the system must include a mismatch in the capacitance of the SMs. By ignoring the nonlinearities, the differential equation of the capacitor voltages in the upper arm of the phase a can be expressed as

$$(C + \Delta C)\frac{dv_{cia}}{dt} = S_{ia} i_{ua} \tag{33}$$

where ΔC is the mismatch for the capacitance of SMs, derived by the multiplication of λ and C. The discretized form of (33) can be written as

$$v_{cia}(k+1) = v_{cia}(k) + \frac{1}{C+\Delta C} T_s S_{ia}(k) i_{ua}(k). \tag{34}$$

The voltage error is caused by the term $\frac{1}{C+\Delta C}$, which can be approximated by a third-order Taylor series as

$$\frac{1}{C+\Delta C} = \sum_{n=0}^{\infty}\frac{\lambda^n(-1)^n}{C} = \frac{1}{C}\left(-\lambda^3 + \lambda^2 - \lambda + 1\right). \tag{35}$$

From (34) and (35), the lumped disturbance is obtained as

$$\xi(k) = -\frac{T_s}{C} A S_{ua}(k) i_{ua}(k) \tag{36}$$

where $A = (\lambda^3 - \lambda^2 + \lambda)$. In this study, λ is equal to $\pm 15\%$. The Kalman Filter (KF) is designed to estimate the lumped

disturbance. The dynamic equation of the disturbance observer is expressed as:

$$\dot{\hat{x}}(t) = \Phi\hat{x}(t) + \mathrm{G}u(t) + \Phi\hat{x}(t) + L(y_s - C\hat{x}(t)) \quad (37)$$

where Φ and G are both available from linear modeling. $\hat{x}(t)$ is the estimated state variable, y_s is the output equation of the system, and L is the gain matrix. According to (34) and (37), the state-space equation of the Kalman filter-based observer is attained as

$$\begin{cases} \begin{bmatrix} \hat{v}_{cia}(k) \\ \hat{\xi}(k) \end{bmatrix} = \Phi \begin{bmatrix} \hat{v}_{cia}(k-1) \\ \hat{\xi}(k-1) \end{bmatrix} + GS_{ia}(k)i_{ua}(k) \\ \qquad\qquad +K(v_{cia}(k-1) - C\hat{v}_{cia}(k-1)) \\ y(k) = C \begin{bmatrix} \hat{v}_{cia}(k) \\ \xi(k) \end{bmatrix}, C = [0\ 1] \end{cases} \quad (38)$$

where $\Phi = [1 \quad -T_s/C]^T$ and $G = [0 \quad T_s/C]^T$. The $\hat{\xi}(k)$ is the normal distribution with zero mean. Covariance matrix Q, and measurement covariance R are used in calculating the gain of the observer, formulated as

$$L = P_{\mathrm{k}}^{-} C^T (C P_{\mathrm{k}}^{-} C^T + R)^{-1} \quad (39)$$

where P_k^- is the prior estimate error covariance matrix obtained as

$$\begin{cases} P_{\mathrm{k}}^{-} = \Phi\hat{P}_{k-1}\Phi^T + Q \\ P_k = (1 - LC)P_{\mathrm{k}}^{-} \end{cases}. \quad (40)$$

The MPC is responsible for rejecting the estimated disturbance; hence, the fourth term is defined as

$$J_4 = w_4\left|\xi^*(k+1) - \xi_p^*(k+1)\right|^2 \quad (41)$$

where $\hat{\xi}^*(k+1)$ is the reference for the estimated lumped disturbance, which is set to zero, as it has to be rejected.

E.Stability analysis of the observer

In this subsection, the stability analysis of the observer is verified. First, the error dynamics of the estimation is defined as,

$$\tilde{\xi}(k) = \xi(k) - \hat{\xi}(k). \quad (42)$$

Two assumptions are considered. First, the uncertain terms are bounded, and secondly, they change at a slow rate; therefore, we have,

$$\tilde{\xi}(k) = \tilde{\xi}(k-1). \quad (43)$$

Taking into account these assumptions and substituting (36) and (38) into (42), the dynamic error is obtained as,

$$\tilde{\xi}(k) = -\frac{T_s}{C} A(S_{ia}(k)i_{ua}(k) - S_{ia}(k-1)\,\hat{i}_{ua}(k-1)) \quad (44)$$

To show the tendency of $\tilde{\xi}(k)$to approach zero, a Lyapunov function candidate is developed as follows,

$$\begin{cases} V(k) = \tilde{\xi}^T(k)\tilde{\xi}(k) \\ \Delta V(k) = V(k+1) - V(k) \end{cases}. \quad (45)$$

Substituting (44) into (45), the Lyapunov function is obtained as follows,

$$\Delta V(k) = -\left(\frac{T_s}{C}\right)^2 A^2 \left(\left(S_{ia}(k+1)i_{ua}(k+1) - S_{ia}(k)\hat{i}_{ua}(k)\right)^2 - \left(S_{ia}(k)i_{ua}(k) - S_{ia}(k-1)\hat{i}_{ua}(k-1)\right)^2\right). \quad (46)$$

The expression (46) can be written as,

$$\Delta V(k) = -\left(\frac{T_s}{C}\right)^2 A^2 \left(S^2{}_{ia}(k+1)i^2{}_{ua}(k+1) + S^2{}_{ia}(k)\hat{i}^2{}_{ua}(k) - 2S_{ia}(k+1)S_{ia}(k)\hat{i}_{ua}(k)i_{ua}(k+1) - S^2{}_{ia}(k)i^2{}_{ua}(k) - S^2{}_{ia}(k-1)\hat{i}^2{}_{ua}(k-1) + 2S_{ia}(k)S_{ia}(k-1)\hat{i}_{ua}(k)i_{ua}(k-1)\right). \quad (47)$$

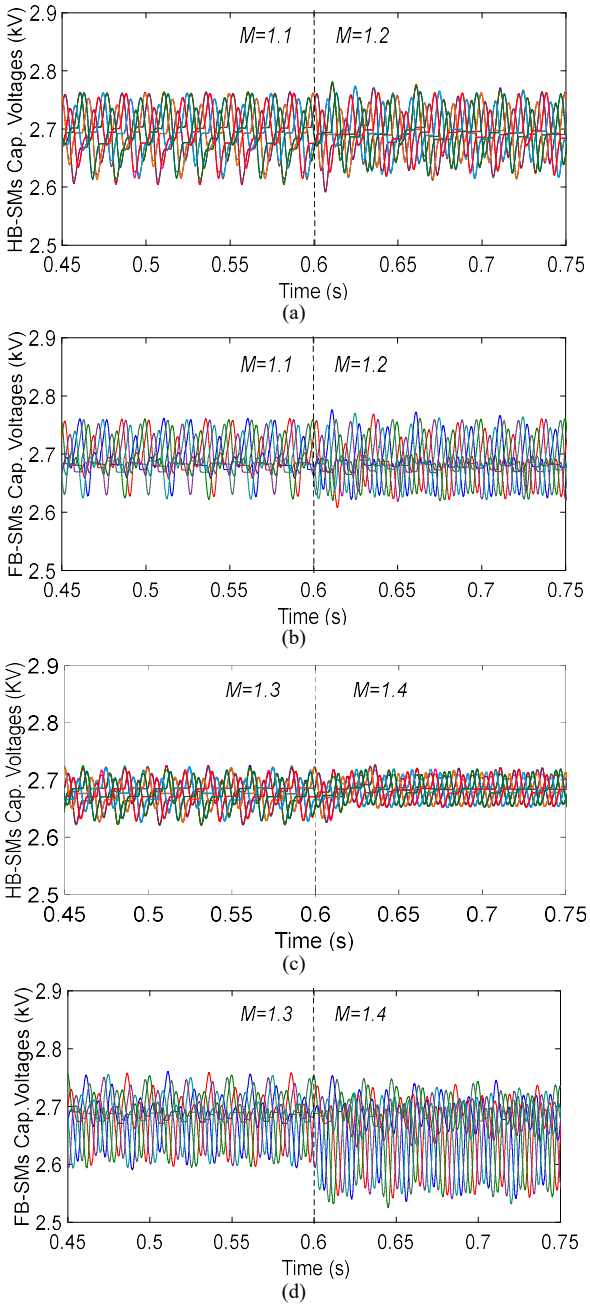

Fig. 3. SMs Capacitors Voltages, (a) Capacitor voltages of HB-SMs at M = 1.1, 1.2, (b) Capacitor voltages of FB-SMs at M = 1.1, 1.2, (c) Capacitor voltages of HB-SMs at M = 1.3, 1.4, (d) Capacitor voltages of FB-SMs at M = 1.3, 1.4.

By relying on the assumptions mentioned earlier, where $S_u = \{-1,0,1\}$, from (46) and (47), one can conclude that ΔV is definitely negative and bounded, indicating the stability of the observer.

IV. Simulation Results

A three-phase 9-L hybrid MMC with a power rate of 1.8 MVA is simulated in MATLAB/SIMULINK to evaluate the performance of the proposed control method. Table II lists the parameters of the simulated hybrid MMC. According to V_{dc} = 8100V and equation (18), the nominal reference voltage for the

TABLE II
HYBRID MMC PARAMETERS IN THE SIMULATION ENVIRONMENT AND EXPERIMENT

PARAMETER	Simulation	Experiment
Number of cells per arm	4	3
Number of FB-SM per arm	1	1
Number of HB-SM per arm	3	2
DC link voltage (V)	8100	180
Nominal voltage reference (V)	2700	90
Switching frequency (kHz)	1	1
Load frequency (Hz)	60	50
Arm inductance (mH)	3	3
SMs capacitance (mF)	2	1.8
Sampling time (μs)	100	50

cells is 2700V. The hybrid ratio is selected at 0.25 using one FB-SM and three HB-SMs in each arm to provide the most demanding balancing condition.

A. Steady-state analysis

This section delves into the steady-state operation of the proposed control method under over-modulation circumstances. The first two scenarios cover approximately 65% of the over-modulation working zone. Fig. 3(a) and 3(b) show the capacitor voltages of the HB- and FB-SMs which are regulated at 2.7 kV with a ripple lower than 6%. Although there is a change in the modulation index at 0.6s, SM voltages remain stable. Fig 3(c) and (d) reveal that the ripple of the FB- and HB-SMs is increased and decreased by boosting the modulation index, respectively. After 0.6s, the highest level of energy oscillation in the FB-SMs and the lowest one in the HB-SMs is observed, which is in accordance with the theoretical analysis in Section II. By turning to $M = 1.4$, the energy variations of the FB-SMs are remarkably supplemented, whereas the opposite is true for the HB-SMs.

Fig. 4(a) depicts the 6-L arm voltages resulting from a conflation of the 3-L bipolar output voltage of the FB-SM and the 4-L unipolar output voltage generated by three HB-SMs. Furthermore, the 9-L three-phase output voltage is illustrated in Fig. 4(b). The total harmonic distortion (THD) and the fundamental component of the output voltages are indicated in Fig. 4(c). The value of the latter is close to 99% of the theoretical expected value from (2). Fig. 4(d) shows the arm currents. Fig. 4(e) shows the three-phase balanced output currents. Finally, Fig. 4(f) illustrates the circulating current containing one-third of the DC link current and fluctuating terms. Fig. 5 shows SMs capacitor voltage ripples of HB- and FB-SMs in accordance with the modulation index. For HB-SMs, r_h indicate how much the capacitors' voltage swings from the average value (ripple). Similarly, r_f is the same for FB-SMs.

B. Dynamic performance analysis

The dynamic performance of the proposed control method is studied under varying circumstances caused by changes in DC link voltage and output power. Fig. 6(a) and (b) show the capacitor voltages in the first scenario, where DC link voltage and output power have changed at 0.3s and 0.45s, respectively. The DC link voltage is reduced from 8100 V to 7290 V, and the output power changed from 1800 kVA to 2000 kVA ($pf = 1$). After approximately 50 ms, the voltages of the HB- and FB-SMs are adjusted at the new voltage reference, 2430 V, as illustrated in Fig. 6(a) and (b). The control system can ensure a proper balancing function at the new operating point. In the second scenario, Fig. 6(c) and (d) illustrate the impact of the new form of redundancy and energy oscillation cancellation in the balancing procedure. Assuming a scenario in which $M = 1.3$, and the power factor is 0.9, Fig. 6(c) and (d) depict the capacitor voltages of one phase as a sample. Primarily, MPC determines the optimal switching states from available redundancies without using its introduced form. In this case, the removal of the fluctuating energy is also inactive (by setting the related weighting factor to zero). All the voltages of the SMs are balanced but with a considerable voltage ripple in the upper arm, whereas in the lower arm, there is also a difference between the HB- and FB-SMs. After 0.5s, the imbalanced energy is eliminated by employing new redundancies and intercession of the energy mitigation section in the control system.

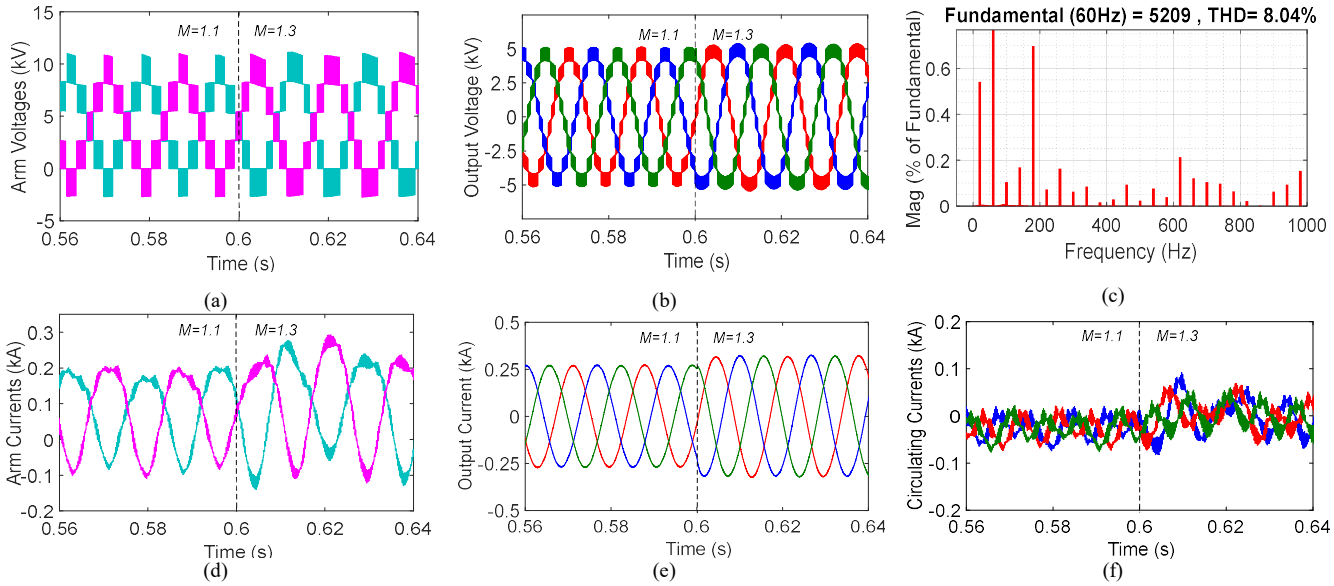

Fig 4. Steady-state performance analysis simulation results, (a) Arm voltages, (b) Three-phase output voltage, (c) Three-phase output voltage fundamental frequency content and THD, (d) Arm currents, (e) Output current, (f) circulating currents.

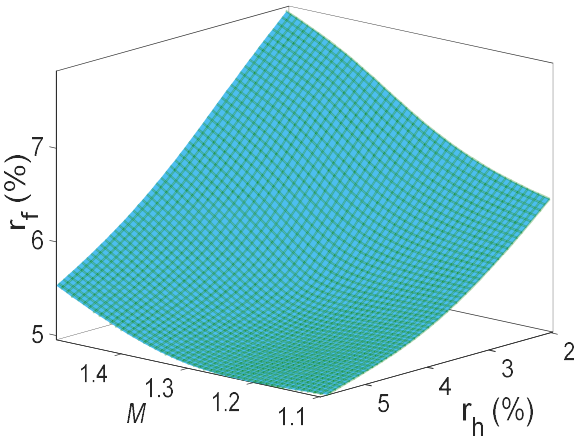

Fig 5. Capacitor voltage ripple of HB- and FB-SMs in accordance with modulation index in the proposed method

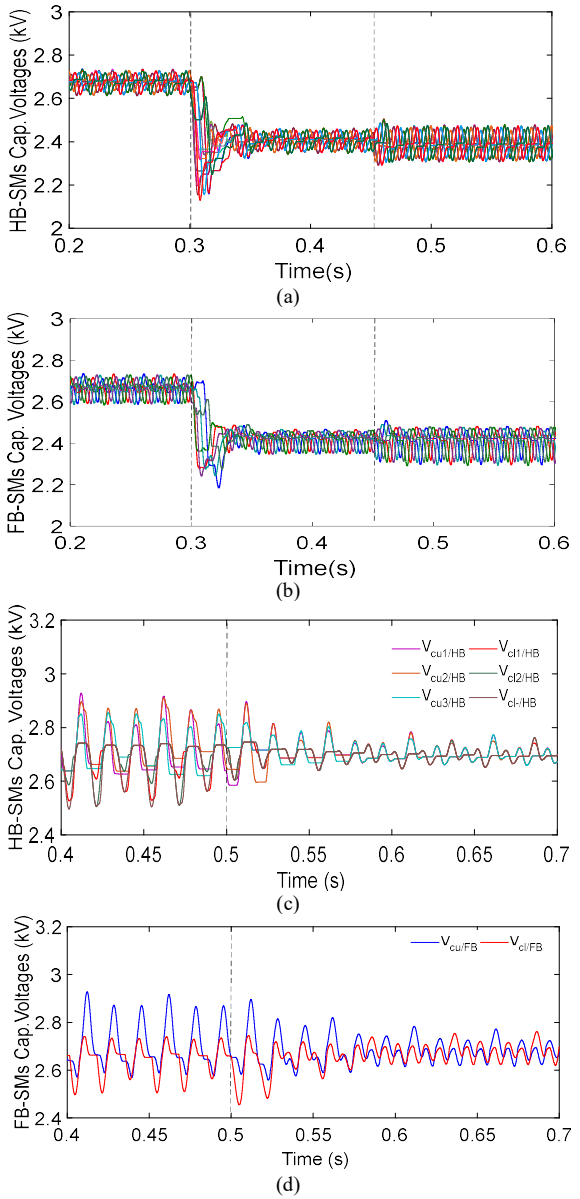

Fig 6. Dynamic performance analysis results for different scenarios: The first scenario: (a) HB-SMs capacitor voltages, (b) FB-SMs capacitor voltages. The second scenario: (c) HB-SMs capacitor voltages, (d) FB-SMs capacitor voltages.

The effectiveness of the proposed control approach is evaluated in comparison with both IMPC and DMPC methods. The modulation index varies from 1.1 to 1.5 in increments of 0.1. Fig. 6(a) shows the performance of the IMPC. While offering acceptable voltage balancing performance for modulation indices below 1.4, a noticeable divergence in capacitor voltages emerges at a modulation index of 1.5. Fig. 6(b) illustrates the capacitor voltages of the HB and FB-SMs in the DMPC method. Similar to IMPC, divergance in the capacitor voltages is apparent at higher modulation indices. The capacitor voltage ripple is higher in the DMPC method. In addition, DMPC demonstrates greater sensitivity to parameter variations and may encounter challenges in achieving convergence. In Fig. 6(c), the capacitor voltages in the proposed method are presented under identical operating conditions. In contrast to IMPC and DMPC, the proposed method offers improved steady-state performance and maintains stability over a broader range of extended regions.

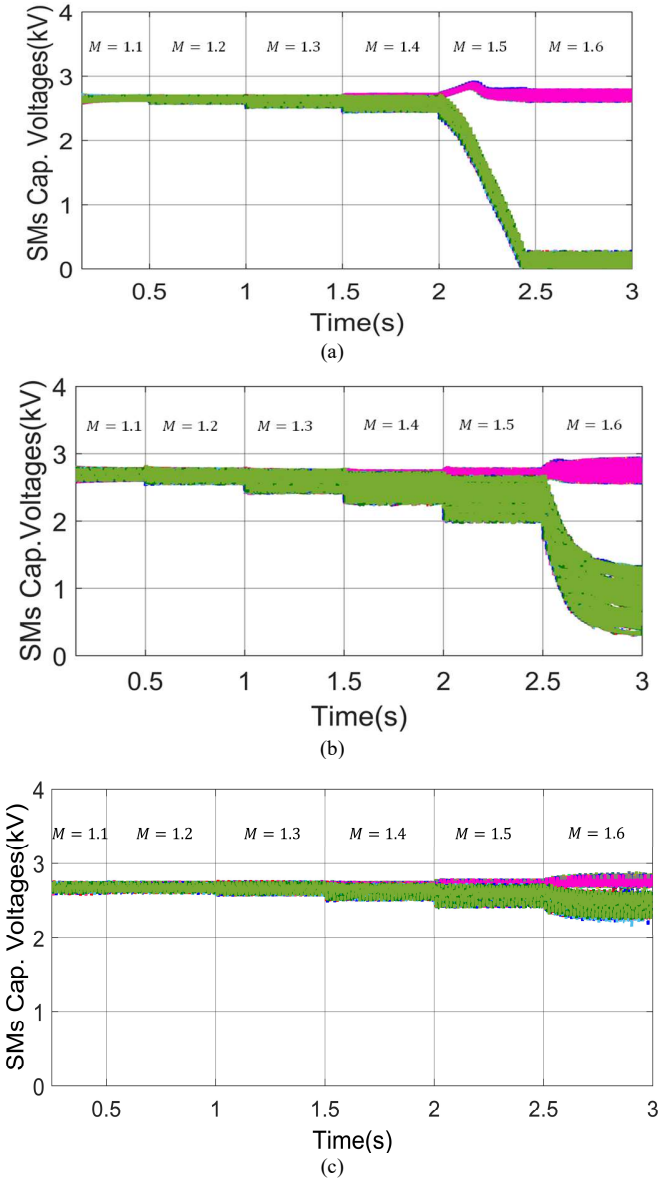

Fig 7. Capacitor voltages under varying modulation indices: (a) IMPC method, (b) DMPC method, (c) Proposed method.

V. Experimental Results

A hybrid MMC prototype with an active power rate of 1 kW is used to validate the proposed method experimentally. The implementation of the control system is based on XILINX Zynq 7000, which integrates FPGA and ARM processors to deliver high-quality functions simultaneously. The FPGA determines the voltage level that must be generated in the arms by comparing the arm voltage references with the carriers based on the EPS-PWM presented in [29]. The MPC is programmed on the ARM, and the switching states are set to meet the control objectives. Fig. 8 illustrates the setup structure, and Table II summarizes the parameters.

Each arm has two HB-SMs and one FB-SM, referring to $h = 0.33$. Therefore, the maximum value of the modulation index is 2. Primarily, the assessment is performed at two modulation indices in the extended operating zone (over-modulation circumstance), including M = 1.45 and M = 1.65. The 3-L bipolar output voltages of the FB-SM and 2-L unipolar outputs of the two HB-SMs yield 5-L arm voltages ranging from -90 V to 270 V, as shown in Fig. 9(a). Fig. 9(b) shows the capacitor voltages of the upper arm at M = 1.45, tuned at 90 V, with negligible steady-state errors and ripples. The high resemblance between the two arm voltages proves the accuracy of balancing in the lower arm.

Fig. 10(a) shows the 9-L output voltage and output current. Compared with the previous scenario, the two extra levels at the AC-side voltage of the converter result from an increase in the modulation index. Furthermore, Fig. 10(b) shows the balanced capacitor voltages of the upper arm at M = 1.65. In this case, the higher engagement of the FB-SM in forming the arm voltages is apparent because of the supplemented negative levels.

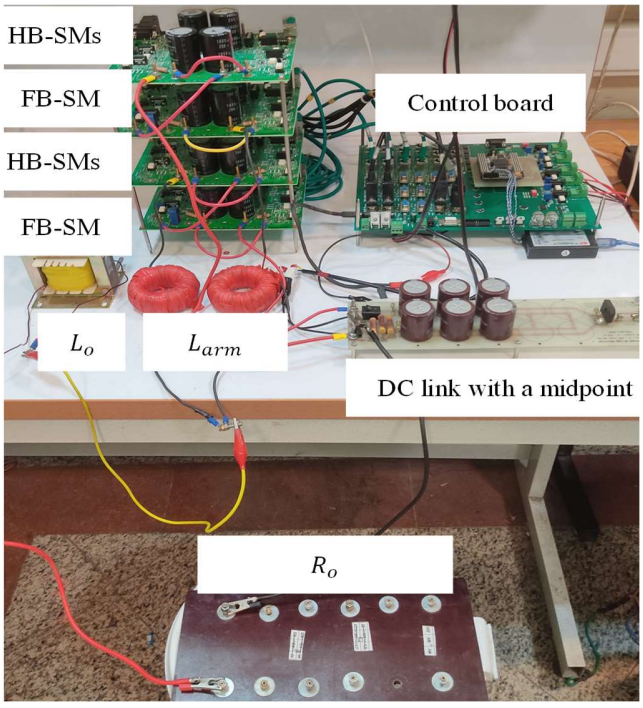

Fig 8. Single-phase hybrid MMC prototype

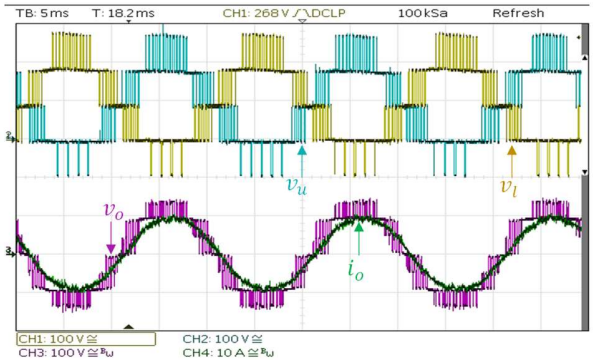

(a)

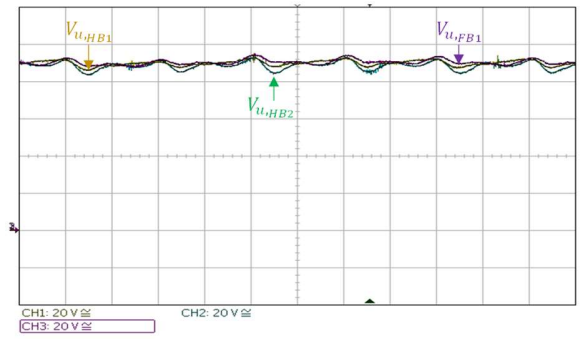

(b)

Fig 9. Experimental test results for M = 1.45: (a) Arm voltages, output voltage and current, (b). Capacitor voltages in the upper arm

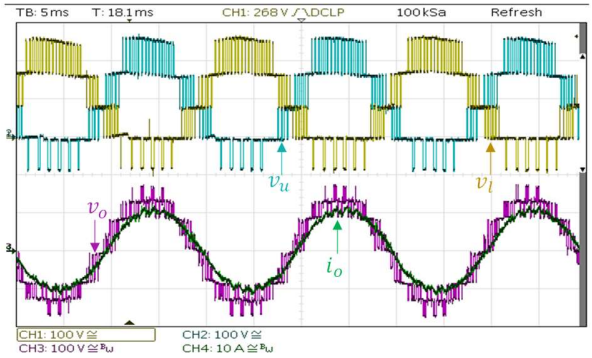

(a)

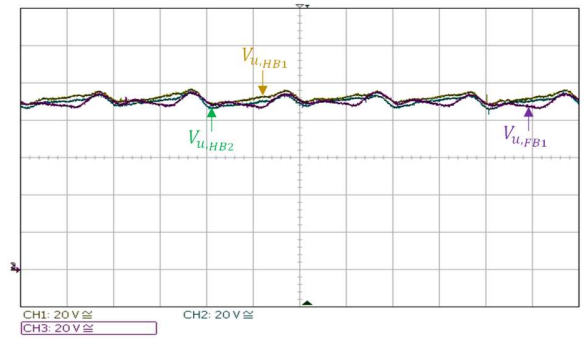

(b)

Fig 10. Experimental test results for M=1.65: (a) Arm voltages, output voltage and current, (b) Capacitor voltages in the upper arm.

To verify the performance of the proposed method in severe conditions, the output voltage frequency is chosen to be 25 Hz

in the next dynamic experiments because under lower frequencies, voltage balancing is more challenging.

Fig. 11(a) and (b) illustrate the effectiveness of the proposed control system when the DC link voltage reduces from 180 to 130V (27% reduction) and restores to 180V (38% increase), respectively. As seen in Fig. 11(a), the initial DC link voltage is 180V, and the nominal voltage of the capacitors is 90V according to (18), where $N = 3$ and $F = 1$. Following the decrease in the DC link voltage to 130V, the capacitor voltages accurately track the new nominal reference. In both cases, as expected, the capacitor voltages are regulated to half of the DC link voltage owing to the modulation method employed. The proposed control system exhibits the same behavior when the scenario is repeated in reverse, as shown in Fig. 10(b). It is worth mentioning that the DC power supply is changed by ramping smoothly over 100 ms.

Fig. 12(a) and (b) illustrate the capacitor voltages of two HB-SMs and one FB-SM in the upper arm and the output current response to a 100% load increase and 50% load reduction, respectively. The control system consistently upholds its performance even when faced with fluctuations in load conditions. The more fluctuating capacitor voltage derives from the lower output frequency. Additionally, Fig. 12(c) and (d) contain the arm voltages, output voltage, and current during load changes.

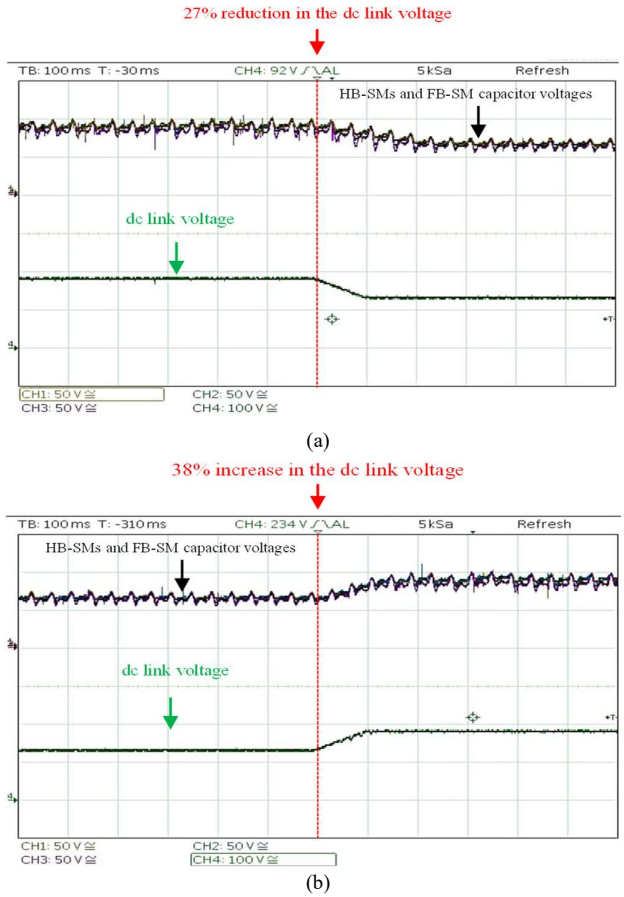

Fig 11. Dynamic behavior of the system in the first scenario: (a) Capacitor voltages under 27% reduction in the DC link voltage, (b) Capacitor voltages under 38% increase in the DC link voltage.

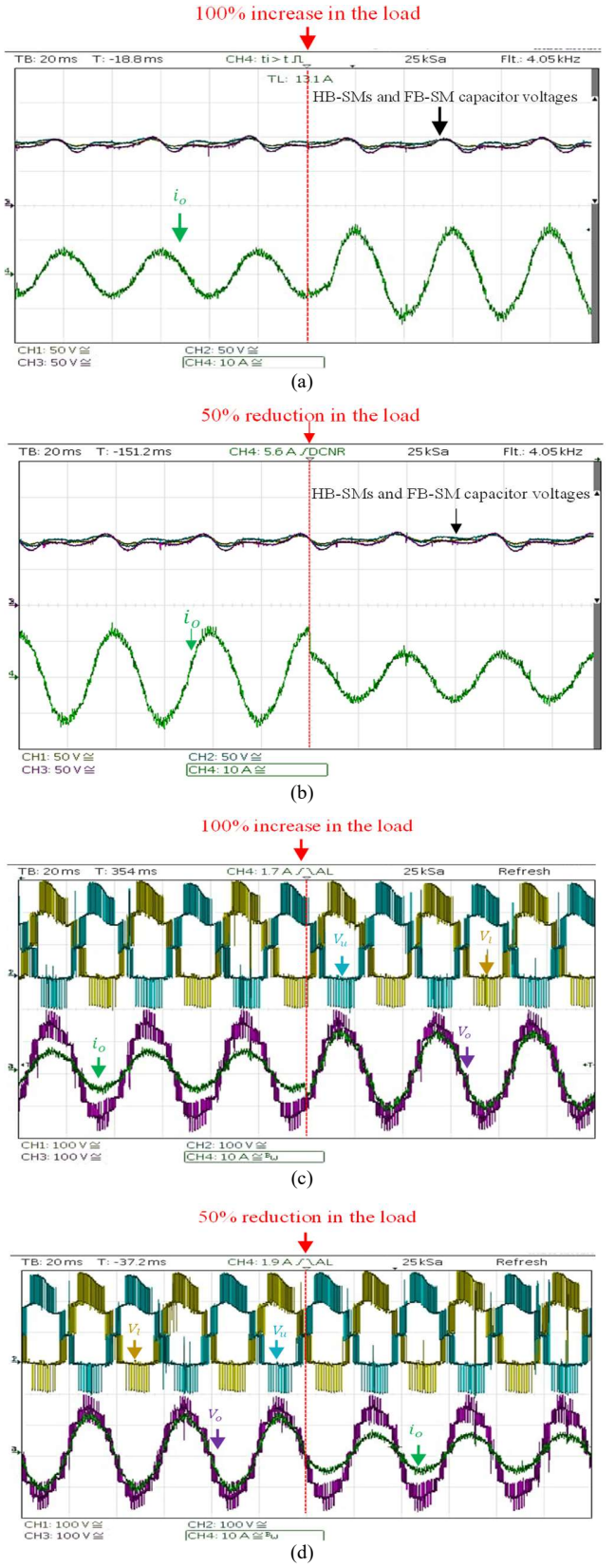

Fig. 12. Dynamic behavior of the system in the second scenario: (a) Capacitor voltages during a 100% increase in the load, (b) Capacitor voltages during a 50% decrease in the load, (c) The arm voltages, output voltage, and current during 100% increase in the load, (d) The arm voltages, output voltage and current during 50% decrease in the load

TABLE III
COMPARISON OF THE PROPOSED METHOD WITH INDIRECT MPC AND DIRECT MPC IN EXPERIMENTS

Criterion	M	Indirect Model Predictive Control (IMPC)	Direct Model Predictive Control (DMPC)	Proposed method
Tracking error	1.2.	e_f = 4.4% e_h =2.1%	e_f =3.8% e_h =2.4%	e_f = 3% e_h =2.4%
	1.4	e_f =2.2% e_h =2.1%	e_f =2.2% e_h =3%	e_f =2.5% e_h =3%
	1.6	Unstable	e_f =1.1% e_h =5%	e_f =1.5% e_h =3.2%
	1.8	Unstable	Unstable	e_f =4.4% e_h =5%
Deviation between the voltage ripple of HB- and FB-SMs	1.2	Δr ≤ 2%	Δr ≤ 4.5%	Δr ≤ 2%
	1.4			
	1.6			
	1.8			
Total Harmonic Distortion (THD)	1.2	10.2%	14.4%	4.9%
	1.4	9.6%	13.9%	5.4%
	1.6	12.10%	14.8%	5.5%
	1.8	19.9%	15.5%	5.7%
Computational Time		39 µs	75 µs	35µs

C. Comparative study

This subsection offers an analytical and numerical comparative study in which the performance of the proposed control method is compared with that of IMPC and DMPC in experiments. Similar to the simulation comparative study, the vertical and horizontal energy balancing terms introduced in [30] are also considered. Figures 13(a) to 13(c) depict the capacitor voltages in IMPC, DMPC, and the proposed method, wherein the modulation indices range from 1 to 1.8 in steps of 0.2.

The IMPC maintains balanced capacitor voltages until the modulation index reaches 1.6. However, as the modulation index becomes 1.6, an obvious voltage deviation appears between the HB-SMs and FB-SM capacitor voltages. From Fig. 12(b), it is evident that the voltage divergence among the capacitor voltages in DMPC commences after *M* reaches 1.6 and becomes increasingly pronounced as *M* approaches 1.8. Fig. 12(c) shows the capacitor voltages of the HB-SMs and FB-SM in the proposed method. Notably, the proposed balancing method keeps the capacitor voltages balanced even under higher modulation indices, such as $M = 1.6$ and $M = 1.8$.

To have a more precise comparison, a comprehensive numerical analysis was conducted based on the recorded data of the discussed methods using the oscilloscope in CSV files and imported in MATLAB/SIMULINK. The findings are listed in Table III. The analysis encompasses various aspects, including tracking error, deviation between the ripples of the HB-SMs and FB-SM, output current total harmonic distortion (THD), and computational time.

The tracking error (the percent of deviation of the average capacitor voltage from the reference value) is defined by e_f and e_h for FB-SMs and HB-SMs, respectively. Moreover, Δr is the absolute difference between r_h and r_f, two factors that have been previously explained. While in the proposed method and IMPC, Δr is less than 2%, the DMPC has the highest amount of Δr, with 4.5%. The computational time (the time when the ARM processor in the Zynq ™ 7000 executes the written code) is derived from setting a bit at the beginning of the code and resetting at the end of the code. It is observed that the execution time of the proposed method is less than that of the two other methods. The main reason is that implementing the Enhanced PWM of the proposed method, which determines the desired output voltage, is performed in the FPGA section of Zynq ™ 7000 and thus has no computational burden on the software part. Furthermore, in IMPC, a sorting algorithm is carried out, which takes almost 13µs of the computational time.

Because of the higher computational time required for DMPC, the sampling time for DMPC was set to be 100 µs. In contrast, IMPC and the proposed method utilize a shorter sampling time, i.e., 50 µs. Consequently, the higher sampling time of the DMPC causes higher distortions, resulting in an increased THD. The proposed method offers improved output current quality performance over a wider range of extended working regions.

VI. CONCLUSION

This paper proposes an innovative control strategy for capacitor voltage balancing within the overmodulation range of hybrid MMCs. This approach is grounded in MPC and enhanced phase-shift PWM, augmented by a supplementary observer that employs a Kalman filter. The core objective is to effectively address the voltage imbalances that manifest across the extended operational spectrum of hybrid MMCs, focusing mainly on modulation indices that exceed 1. By exploiting the ability to generate negative voltage levels in the arm voltages, the proposed method introduces a new redundancy approach for flexibly employing FB-SMs, thereby ensuring alignment with the control objectives of the cost function. The devised cost function encompasses various components, including voltage balance optimization for both HB-SMs and FB-SMs (inter-cell balance), minimization of SMs voltage fluctuations (inter-leg voltage equilibrium), and a compensatory factor that accounts for disturbances in the SMs capacitance. The efficacy of this approach was validated through simulations using

MATLAB/SIMULINK and experimental results obtained from a hardware prototype.

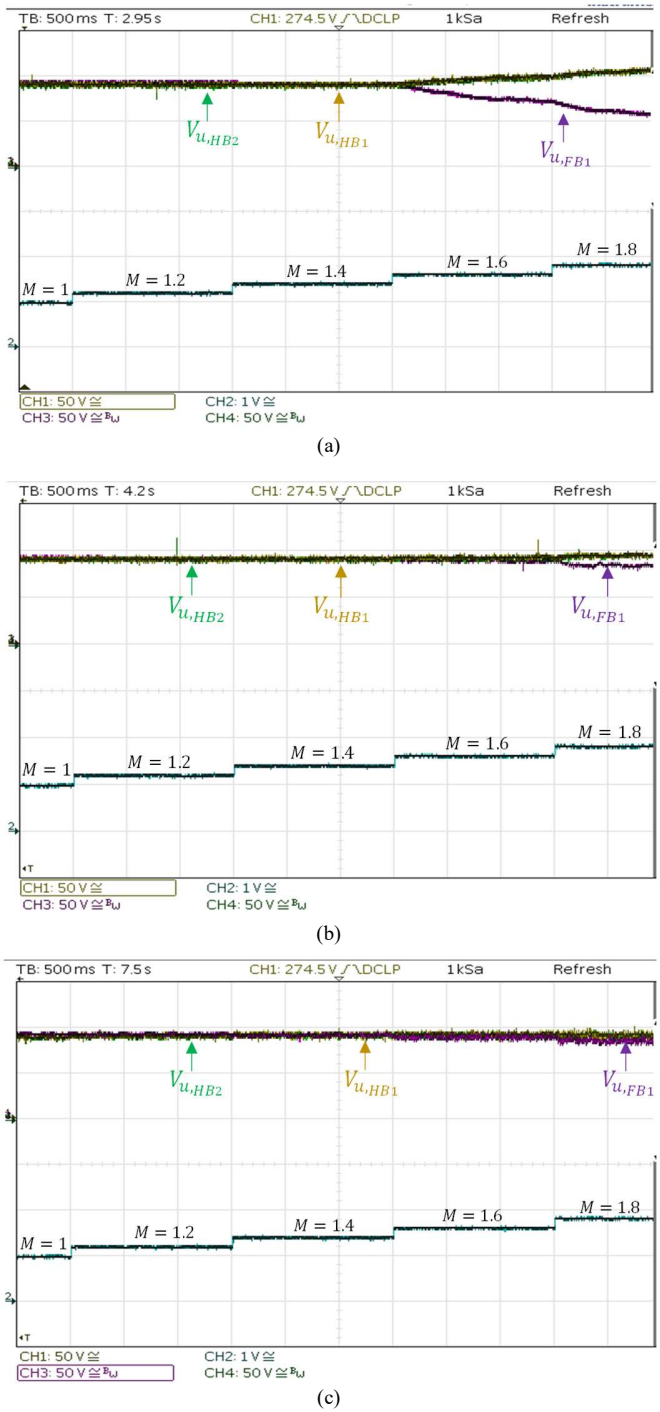

Fig 13. Capacitor voltages of HB-SMs and FB-SM under overmodulation circumstances in the IMPC, DMPC, and proposed methods: (a) capacitor voltages in the IMPC method, (b) capacitor voltages in the DMPC method, and (c) capacitor voltages in the proposed method.

REFERENCES

[1] M. Priya, P. Ponnambalam, and K. Muralikumar, "Modular-multilevel converter topologies and applications – a review," *IET Power Electron.*, vol. 12, no. 2, pp. 170–183, Feb. 2019.

[2] K. Sharifabadi, L. Harnefors, H.-P. Nee, S. Norrga, and R. Teodorescu, *Design, Control, and Application of Modular Multilevel Converters for HVDC Transmission Systems*. John Wiley & Sons, 2016, pp. 98–112.

[3] J. A. Ansari, C. Liu, and S. A. Khan, "MMC Based MTDC Grids: A Detailed Review on Issues and Challenges for Operation, Control and Protection Schemes," *IEEE Access*, vol. 8, pp. 168154–168165, 2020.

[4] S. Du, A. Dekka, B. Wu, and N. Zargari, *Modular Multilevel Converters: Analysis, Control, and Applications*. John Wiley & Sons, 2018, pp. 47–81.

[5] M. A. Perez, S. Ceballos, G. Konstantinou, J. Pou, and R. P. Aguilera, "Modular Multilevel Converters: Recent Achievements and Challenges," *IEEE Open Journal of the Industrial Electronics Society*, vol. 2, pp. 224–239, 2021.

[6] M. Basić and D. Dujić, "Hybrid modular multilevel converter for variable DC link voltage operation," *CPSS Transactions on Power Electronics and Applications*, vol. 6, no. 2, pp. 178–190, Jun. 2021.

[7] S. Cui and S.-K. Sul, "A comprehensive DC short-circuit fault ride through strategy of hybrid modular multilevel converters (MMCs) for overhead line transmission," *IEEE Trans. Power Electron.*, vol. 31, no. 11, pp. 7780–7796, Nov. 2016.

[8] X. Zhao, J. Ding, J. Xu, and J. Yuan, "Hybrid MMC with Low Voltage Operations and DC Fault Ride-through Capabilities Based on Auxiliary Full-bridge Converter," *CSEE Journal of Power and Energy Systems*, vol. 8, no. 3, pp. 864–871, May 2022.

[9] W. Xiang, S. Yang, L. Xu, J. Zhang, W. Lin, and J. Wen, "A Transient Voltage-Based DC Fault Line Protection Scheme for MMC-Based DC Grid Embedding DC Breakers," *IEEE Trans. Power Delivery*, vol. 34, no. 1, pp. 334–345, Feb. 2019.

[10] R. Zeng, L. Xu, L. Yao, and B. W. Williams, "Design and Operation of a Hybrid Modular Multilevel Converter," *IEEE Trans. Power Electron.*, vol. 30, no. 3, pp. 1137–1146, Mar. 2015.

[11] Y. Dong, J. Tang, H. Yang, W. Li, and X. He, "Capacitor Voltage Balance Control of Hybrid Modular Multilevel Converters With Second- Order Circulating Current Injection," *IEEE Journal of Emerging and Selected Topics in Power Electronics*, vol. 7, no. 1, pp. 157–167, Mar. 2019.

[12] W. Lin, D. Jovcic, S. Nguefeu *et al.*, "Full-bridge MMC converter optimal design to HVDC operational requirements," *IEEE Transactions on Power Delivery,* vol. 31, no. 3, pp. 1342-1350, Aug. 2015.

[13] X. Fang, G. Li, C. Chen, J. Xiong, and K. Zhang, "An Auxiliary Circuit Enhancing DC Fault Clearing Capability of Hybrid MMCs With Low Proportion of FB-SMs," *IEEE Trans. Power Electron.*, vol. 37, no. 10, pp. 11491–11496, Oct. 2022.

[14] X. Fang, G. Li, C. Chen, D. Wang, J. Xiong, and K. Zhang, "An Energy Absorbing Method for Hybrid MMCs to Avoid Full-Bridge Submodule Overvoltage During DC Fault Blocking," *IEEE Trans. Power Electron.*, vol. 37, no. 5, pp. 4947–4951, May 2022.

[15] L. Lin, Y. Lin, C. Xu, and Y. Chen, "Comprehensive Analysis of Capacitor Voltage Fluctuation and Capacitance Design for Submodules in Hybrid Modular Multilevel Converter With Boosted Modulation Index," *IEEE Journal of Emerging and Selected Topics in Power Electronics*, vol. 7, no. 4, pp. 2369–2383, Dec. 2019.

[16] M. Li, N. Dong, X. Chang, H. Yang, and R. Zhao, "Analysis and Suppression of Capacitor Voltage Ripple for Hybrid MMCs Under Boosted AC Voltage Conditions," *IEEE Journal of Emerging and Selected Topics in Power Electronics*, vol. 11, no. 4, pp. 3775–3787, Aug. 2023.

[17] K. Llves, S. Norrga, and H. P. Nee, "On energy variations in modular multilevel converters with full-bridge submodules for AC–DC and AC–AC applications," in Proc. 15th Eur. Conf. Power Electron. Appl., Sep. 2013, pp. 1–10.

[18] N. Tashakor, F. Iraji, and S. M. Goetz, "Low-Frequency Scheduler for Optimal Conduction Loss in Series/Parallel Modular Multilevel Converters," *IEEE Trans. Power Electron.*, vol. 37, no. 3, pp. 2551–2561, Mar. 2022.

[19] Y. Zhang, J. Zhang, F. Deng, Z. Xu, and J. Zhao, "Hybrid Modular Multilevel Converter With Self-Balancing Structure," *IEEE Trans. Ind. Appl.*, vol. 57, no. 5, pp. 5039–5051, Sep. 2021.

[20] V. Hofmann and M.-M. Bakran, "A capacitor voltage balancing algorithm for hybrid modular multilevel converters in HVDC applications," in *2017 IEEE 12th International Conference on Power Electronics and Drive Systems (PEDS)*, Dec. 2017, pp. 691–696.

[21] J. Zhang, J. Liu, J. Liu, W. Fang, J. Hou, and Y. Dong, "Modified capacitor voltage balancing sorting algorithm for modular multilevel converter," *J. Eng. (Stevenage)*, vol. 2019, no. 16, pp. 3315–3319, Mar. 2019.

[22] H. Mohamed Ismail and S. Kaliyaperumal, "Enhanced Voltage Sorting Algorithm for Balancing the Capacitor Voltage in Modular Multilevel Converter," *IEEE Access*, vol. 9, pp. 167489–167502, 2021.
[23] M. Lu, J. Hu, R. Zeng, W. Li, and L. Lin, "Imbalance Mechanism and Balanced Control of Capacitor Voltage for a Hybrid Modular Multilevel Converter," *IEEE Trans. Power Electron.*, vol. 33, no. 7, pp. 5686–5696, Jul. 2018.
[24] M. Lu, J. Hu, R. Zeng, and Z. He, "Fundamental-Frequency Reactive Circulating Current Injection for Capacitor Voltage Balancing in Hybrid-MMC HVDC Systems During Riding Through PTG Faults," *IEEE Trans. Power Delivery*, vol. 33, no. 3, pp. 1348–1357, Jun. 2018.
[25] P. Hu, R. Teodorescu, and J. M. Guerrero, "Negative-Sequence Second-Order Circulating Current Injection for Hybrid MMC Under Over-Modulation Conditions," *IEEE Journal of Emerging and Selected Topics in Power Electronics*, vol. 8, no. 3, pp. 2508–2519, Sep. 2020.
[26] J. Xu *et al.*, "Dual Harmonic Injection for Reducing the Submodule Capacitor Voltage Ripples of Hybrid MMC," *IEEE Journal of Emerging and Selected Topics in Power Electronics*, vol. 9, no. 3, pp. 3622–3633, Jun. 2021.
[27] X. Xifeng, L. Yuqiang, and Z. Jianglin, "Research on model predictive control for modular multilevel converter," in *2017 IEEE 2nd Information Technology, Networking, Electronic and Automation Control Conference (ITNEC)*, Dec. 2017, pp. 272–276.
[28] A. Dekka, B. Wu, V. Yaramasu, R. L. Fuentes, and N. R. Zargari, "Model Predictive Control of High-Power Modular Multilevel Converters—An Overview," *IEEE Journal of Emerging and Selected Topics in Power Electronics*, vol. 7, no. 1, pp. 168–183, Mar. 2019.
[29] C. Xu, L. Lin, T. Yin, and J. Hu, "An Improved Phase-Shifted-Carrier Technique for Hybrid Modular Multilevel Converter With Boosted Modulation Index," *IEEE Trans. Power Electron.*, vol. 35, no. 2, pp. 1340–1352, Feb. 2020.
[30] W. Tian, X. Gao, and R. Kennel, "Model predictive control of modular multilevel converters with independent arm-balancing control," in 2019 IEEE International Symposium on Predictive Control of Electrical Drives and Power Electronics (PRECEDE), 2019, pp. 1–5.

Amin Hashemi Zadeh obtained his B.Sc. degree in Electrical Engineering from Imam Khomeini International University, Ghazvin, Iran in 2018, and his M.Sc. degree in Electrical Engineering from the University of Tehran, Tehran, Iran in 2021. Currently, he is pursuing his Ph.D. degree at the Technical University of Kaiserslautern in Germany. His research interests lie in the areas of multilevel power converters and motor drives.

Saeid Ahmadi received the B.Sc. and M.Sc. degrees in electrical engineering with honors from the University of Tehran, Tehran, Iran, in 2018 and 2020, respectively. He is currently pursuing the Ph.D. degree in electrical engineering at University of Tehran, Tehran, Iran. His current research interests include advanced control for modular multilevel converters, and HVDC systems.

Yousef Neyshabouri received the B.Sc., M.Sc. and Ph.D. degrees, all in electrical engineering from the University of Tehran, Tehran, Iran, in 2011, 2013 and 2018, respectively. He is currently an Associate Professor with the Faculty of Electrical and Computer Engineering, Urmia University, Urmia, Iran. His current research interests include multilevel power converters and their application in FACTS and renewable energy systems.

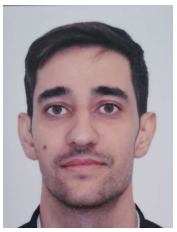

Ehsan Asadi received the B.Sc. degree in electrical engineering from Isfahan University of Technology, Isfahan, Iran, in 2017, and the M.Sc. degree in electrical engineering from the University of Tehran, Tehran, Iran, in 2020. He is currently a Research Assistant at the School of Electrical and Computer Engineering, University of Tehran. His research interests include design and modeling of power electronic converters, photovoltaics systems, and applications of power electronics in power systems.

Hossein Iman-Eini received the Ph.D. degree in electrical engineering jointly from the University of Tehran, Tehran, Iran, and the Grenoble Alpes University, Grenoble, France, in 2009. He is a Professor of Electrical Engineering at the School of Electrical and Computer Engineering, University of Tehran. He currently follows a Heisenberg position in Chair of Power Electronics at Kiel University, Germany. His research interests include power electronics and applications of power electronics in power systems/grids

MARCO LISERRE (S'00-M'02-SM'07-F'13) obtained the MSc and PhD degrees in Electrical Engineering from the Politecnico di Bari in 1998 and 2002 respectively. He has been Associate Professor at the Politecnico di Bari and, since 2012, Professor of Reliable Power Electronics at Aalborg University (Denmark). Since 2013 he is Full Professor and holds the Chair of Power Electronics at the University of Kiel (Germany). He has been offered and declined professorships at several universities. He has published more than 700 technical papers (1/3 of them in international refereed journals), one book and 7 granted patents (4 with companies). These works have received more than 50,000 citations. Marco Liserre was selected as an Highly Cited Researcher in the field of Engineering (Clarivate Web of Science) from 2014 to 2021. Several of his students (MSc, PhD and post-docs) are in leading positions in industry and universities worldwide. In 2023, he joined the Fraunhofer ISIT on a part-time basis as deputy director and director of the new division "Electronic Energy Systems", as well as of the Kiel branch of the Fraunhofer ISIT. He is a member of IAS, PELS, PES and IES. He has served all these societies in various capacities. In PELS, he is Co-Editor of the IEEE Open Access Journal in Power Electronics and Technical Committee Chairman of the Committee on Electronic Power Grid Systems. He has co-chaired several IEEE conferences being several times Chairman. He has received 16 awards from IEEE, PCIM and EPE-PEMC, including the prestigious 2018 IEEE-IES Mittelmann Achievement Award and the 2023 IEEE-PELS R. David Middlebrook Achievement Award. In 2023, he was awarded the title of "Ufficiale" by the President of the Italian Republic. In 2025 he will be Chairman of Powertech 2025 in Kiel.